


Image charge effect in layered materials: Implications for the interlayer coupling in MoS₂P. Marauhn¹ and M. Rohlfing*Institut für Festkörperteorie, Westfälische Wilhelms-Universität Münster, 48149 Münster, Germany* (Received 14 January 2023; revised 12 March 2023; accepted 20 March 2023; published 7 April 2023)

The electronic and optical properties of layered materials, such as transition metal dichalcogenides, can be strongly affected by their dielectric environment—this phenomenon is also known as the image charge effect. In multilayers, the stacked crystal structure implies a layer-dependent variation of the image charge effect. However, this variation and its implications on the interlayer coupling are heretofore not well understood. Here, we show that the variation of dielectric screening effects in layered materials can be described by a macroscopic dielectric continuum model within classical electrostatics. We present an efficient method that incorporates this effect in electronic structure calculations. The present method is based on semi-empirical tight-binding and amenable to use for large-scale systems. By applying this method to multilayer MoS₂, we find an energetic decoupling of the surface layer—at the K point of the Brillouin zone—which leads to the formation of a surface-layer band gap. More generally, our calculations reveal that the image charge effect can cause spatial modulation of the interlayer coupling by changing the band alignment between the layers.

DOI: [10.1103/PhysRevB.107.155407](https://doi.org/10.1103/PhysRevB.107.155407)**I. INTRODUCTION**

Interlayer coupling plays a central role in determining the properties of layered materials [1,2]. In transition metal dichalcogenides (TMDCs), for example, interlayer coupling leads to a crossover from a direct band gap in the monolayer to an indirect band gap in multilayer materials [3–5]. Recently, much effort has been put into actively controlling interlayer coupling in layered materials to tailor their electronic [6,7] and optical properties [8]. A comprehensive understanding of the mechanisms underlying interlayer coupling is therefore of great importance.

Key parameters that determine the interlayer coupling are the interlayer hopping t , and the band offset Δ (see Fig. 1). While interlayer hopping arises from the quantum-mechanical interaction between orbitals on adjacent layers, the band offset generally depends on several mechanisms, including dielectric screening effects. In fact, screening effects play a crucial role in layered materials. The atomically thin structure of the layers is intrinsically linked to a weak screening [9,10]. Dielectric polarization of their surroundings can therefore considerably modify the Coulomb interaction inside the layers, thus shifting their energy levels. This phenomenon, also called the *image charge effect*, is well known in the context of nanostructures [11,12], and molecules on surfaces [13,14]. Several studies, experimental and theoretical, have shown that the electronic and optical properties of layered materials strongly depend on their dielectric environment (vacuum, a substrate, or adjacent layers) [15–26]. Yet, most studies on screening effects focus on monolayers, while multilayer materials are rarely addressed. Notably, the stacked structure of multilayer materials suggests a layer-dependent variation of

the screening effects, affecting the band alignment between the layers. Thus, it is important to investigate the variation of screening effects in multilayer materials and analyze their role in interlayer coupling. In fact, Winther and Thygesen reported a spatially varying band gap in multilayer hexagonal boron nitride [27]. However, while electrostatic interactions between the layers were taken into account, interlayer hopping has been disregarded.

A suitable theoretical framework that captures the relevant physical mechanisms discussed above is given by many-body perturbation theory. The GW method [28–30] has proven to be an accurate tool for calculating quasiparticle (QP) energies, i.e., electron addition and removal energies, including energy level alignments [13,14]. In particular, dielectric polarization effects are included via the screened Coulomb interaction in terms of an electron self-energy. However, applying the GW method to multilayer materials is a formidable task due to the high computational cost. A possible way to overcome this difficulty is to decompose the electron self-energy and only retain those corrections that arise from dielectric polarization effects of the environment. For silicon nanocrystals, Allan, Delerue, and Lannoo have shown that these self-energy corrections can be computed with good accuracy by using an image potential derived from a continuum model [31–33]. However, it is not clear whether such a continuum model approach is applicable to layered materials.

In the present paper, we discuss a computationally efficient method to capture the image charge effect in semi-empirical band structure calculations, which we call the TB+ $\delta\Sigma$ method. This method combines tight binding (TB) with a self-energy $\delta\Sigma$, derived in the GW approximation, that solely accounts for the image charge effect. Focusing on layered materials, we show that the interaction potential of $\delta\Sigma$ can be well described by an image potential derived from an anisotropic continuum model. With freestanding

*p.marauhn@wwu.de

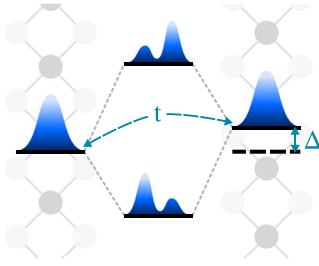


FIG. 1. Schematic illustration of the interlayer coupling between two electronic states on adjacent layers. The coupling modifies the orbital compositions and leads to an energy splitting between the interacting states. Relevant parameters that determine the coupling are the interlayer hopping t and the band offset Δ .

molybdenum disulfide (MoS_2) as a prototypical example, we investigate the variation of image-charge induced self-energy corrections in multilayer materials as a function of layer position and number of layers. We then use the TB+ $\delta\Sigma$ method to show how the image charge effect modifies the band alignment in multilayer materials, thereby affecting the coupling between the layers. Specifically for the case of multilayer MoS_2 in vacuum, we show that the image charge effect leads to an energetic decoupling of the outermost layer (surface layer) at the K point of the Brillouin zone.

The present paper is organized as follows: In Sec. II, we present the theoretical method used in this paper. Section III is devoted to the screened image interaction in layered materials. In Sec. IV, we present results on the electronic structure of mono- and multilayer MoS_2 surrounded by vacuum. We specifically focus on the multilayer, discussing the implications of the image charge effect for the interlayer coupling. Section V concludes this paper with a summary of our main results.

II. THEORETICAL FRAMEWORK

In this section, we present a method for electronic structure calculations based on semi-empirical TB, taking into account the image charge effect within many-body perturbation theory.

First, in Sec. II A, we derive a practical expression for the self-energy caused by the image charge effect—we call it the image self-energy $\delta\Sigma$ —from the electron self-energy in the GW approximation. In the subsequent Sec. II B, we introduce the TB+ $\delta\Sigma$ method used in this paper; an efficient method for electronic structure calculations that includes the image self-energy and is based on semi-empirical TB. Finally, in Sec. II C, we work out the matrix elements of the image self-energy in the framework of (nonorthogonal) semi-empirical TB.

A. Image charge effect within many-body perturbation theory: The image self-energy operator

The central quantity within many-body perturbation theory is the electron self-energy operator. From this operator one can calculate quasiparticle (QP) spectra, i.e., electron addition and removal spectra. In Hedin's GW approximation [28,30],

the electron self-energy operator is given by

$$\Sigma = iGW, \quad (1)$$

where G is the single-particle Green's function and W is the screened Coulomb interaction of the system. Compared to the case of an infinite bulk crystal, the interfaces of a system can introduce drastical modifications in the screened interaction and hence the electron self-energy. These modifications result from the difference in the polarizability of the environment (vacuum, substrate, etc.) compared to the bulk crystal.

In order to quantify the effect of the environment's dielectric polarizability, we rewrite the screened Coulomb interaction of the system as follows:

$$\begin{aligned} W &= W_{\text{bulk}} + (W - W_{\text{bulk}}) \\ &= W_{\text{bulk}} + W_{\text{im}}, \end{aligned} \quad (2)$$

where W_{bulk} is the interaction with hypothetical screening of the bulk crystal. The second term W_{im} is a correction that accounts for the difference in the dielectric screening between the actual system and its bulk counterpart. This term is entirely due to the dielectric interfaces of the system and hence due to the different polarizability of the environment. Following classical electrodynamics, where the potential of this type of interaction is often calculated using the method of images, we call W_{im} the *screened image interaction*. The separation of the screened Coulomb interaction in Eq. (2) transfers directly to the electron self-energy operator defined in Eq. (1). That is,

$$\begin{aligned} \Sigma &= iGW_{\text{bulk}} + iGW_{\text{im}} \\ &= \Sigma_{\text{bulk}} + \delta\Sigma. \end{aligned} \quad (3)$$

The first term on the right-hand side of Eq. (3) represents the self-energy of the system with hypothetical screening of the bulk crystal. The second term $\delta\Sigma$ is the self-energy due to the environment's dielectric polarizability, or, more precisely due to the different polarizability of the environment compared to the bulk. Since $\delta\Sigma$ describes the image charge effect, we call it the *image self-energy operator*.

Up to this point, we have restricted our discussion to formal relations. In frequency space, the explicit expression for the image self-energy operator reads as

$$\delta\Sigma(\mathbf{r}, \mathbf{r}'; \omega) = \frac{i}{2\pi} \int G(\mathbf{r}, \mathbf{r}'; \omega + \omega') W_{\text{im}}(\mathbf{r}, \mathbf{r}'; \omega') d\omega'. \quad (4)$$

In general, computing this convolution can be a difficult and time-consuming task. To simplify the frequency integration, we adopt the approximation of a statically screened image interaction. Equation (4) can then be written in the form

$$\begin{aligned} \delta\Sigma(\mathbf{r}, \mathbf{r}') &= - \sum_{nk}^{\text{occ.}} \psi_{nk}(\mathbf{r}) \psi_{nk}^*(\mathbf{r}') W_{\text{im}}(\mathbf{r}, \mathbf{r}') \\ &\quad + \frac{1}{2} \delta(\mathbf{r} - \mathbf{r}') W_{\text{im}}(\mathbf{r}, \mathbf{r}'). \end{aligned} \quad (5)$$

This expression is consistent with the static *Coulomb hole plus screened exchange* (COHSEX) approximation introduced by Hedin [28]. It is important to note that we only consider this approximation for the image self-energy $\delta\Sigma$; not for the total electron self-energy Σ . The first term in Eq. (5) represents a screened exchange (SEX) interaction and the second term can

be interpreted as a Coulomb hole (COH). While the Coulomb-hole part is purely local, the screened-exchange part contains nonlocal effects. In order to further simplify the computation of the image self-energy operator, we neglect the nonlocal contributions of the screened image interaction. The image self-energy is thus given by

$$\delta\Sigma(\mathbf{r}, \mathbf{r}') = -\frac{1}{2} \sum_{nk}^{\text{occ.}} \psi_{nk}(\mathbf{r}) \psi_{nk}^*(\mathbf{r}') [W_{\text{im}}(\mathbf{r}) + W_{\text{im}}(\mathbf{r}')] + \frac{1}{4} \delta(\mathbf{r} - \mathbf{r}') [W_{\text{im}}(\mathbf{r}) + W_{\text{im}}(\mathbf{r}')], \quad (6)$$

where $W_{\text{im}}(\mathbf{r}) \equiv W_{\text{im}}(\mathbf{r}, \mathbf{r})$ denotes the *local* contribution of the screened image interaction. For practical calculations, it is useful to express the image self-energy operator as a matrix. In a basis of single-particle states $|n\mathbf{k}\rangle$, the matrix elements of the image self-energy are given by

$$\begin{aligned} \langle n\mathbf{k} | \delta\Sigma | n'\mathbf{k} \rangle &= \frac{1 - f_{n\mathbf{k}} - f_{n'\mathbf{k}}}{2} \langle n\mathbf{k} | W_{\text{im}} | n'\mathbf{k} \rangle \\ &= \begin{cases} -\frac{1}{2} \langle n\mathbf{k} | W_{\text{im}} | n'\mathbf{k} \rangle & \text{for } n, n' \in \text{occ.} \\ +\frac{1}{2} \langle n\mathbf{k} | W_{\text{im}} | n'\mathbf{k} \rangle & \text{for } n, n' \in \text{unocc.} \end{cases}. \quad (7) \end{aligned}$$

Here, $f_{n\mathbf{k}}$ and $f_{n'\mathbf{k}}$ denote the occupation numbers of the single-particle states. These matrix elements correspond to QP corrections resulting from the image charge effect; here we emphasize that they are not intended to give the full QP corrections of the electron self-energy Σ defined in Eq. (1). The physical origin of the image charge effect arises from the difference in the environment's polarizability compared to the bulk crystal of the system. Equation (7) will be central to the TB+ $\delta\Sigma$ method presented in Sec. II B. We note that the expression given in Eq. (7) has already been derived before by Delerue *et al.* [33] and Freysoldt *et al.* [34].

B. The TB+ $\delta\Sigma$ method

We now present a method for calculating the electronic structure that incorporates the renormalization of the Coulomb interaction arising due to the dielectric environment of the system. This method, which we call TB+ $\delta\Sigma$, combines the computational efficiency of semi-empirical TB with the image self-energy $\delta\Sigma$ introduced in the previous section. While other works have used a similar approach [31,33], we extend these works by going beyond a perturbative treatment of the image self-energy. Moreover, we discuss how to calculate the matrix elements of the image self-energy for the general case of a nonorthogonal TB model (see Sec. II C).

In order to motivate the Hamiltonian of the TB+ $\delta\Sigma$ method, we consider the QP Hamiltonian of the GW method. In the usual formulation, with density functional theory (DFT) as starting point, one can formally set up the Hamiltonian [35]

$$\hat{H}^{\text{GW}} = \hat{H}^{\text{DFT}} - V_{\text{xc}} + \Sigma. \quad (8)$$

In the above equation, \hat{H}^{DFT} is the DFT Hamiltonian, V_{xc} is the exchange-correlation potential of \hat{H}^{DFT} , and $\Sigma = i\text{GW}$ is the electron self-energy within GW. According to Sec. II A, we can decompose Σ into the image self-energy $\delta\Sigma$ and the bulk-screened self-energy Σ_{bulk} . The QP Hamiltonian of Eq. (8) can

then be written in the form

$$\hat{H}^{\text{GW}} = \hat{H}^{\text{DFT}} - V_{\text{xc}} + \Sigma_{\text{bulk}} + \delta\Sigma. \quad (9)$$

The starting point of the TB+ $\delta\Sigma$ method is a semi-empirical TB model. Such models are typically constructed on the basis of DFT calculations, meaning $\hat{H}^{\text{TB}} \approx \hat{H}^{\text{DFT}}$. Since we are mainly interested in QP corrections induced by the dielectric environment of the system, we shall neglect the terms $-V_{\text{xc}}$ and Σ_{bulk} in the construction of the TB+ $\delta\Sigma$ Hamiltonian; both terms do not contribute to the effect we want to describe. Hence, in the TB+ $\delta\Sigma$ method, the QP Hamiltonian [Eq. (9)] simplifies to

$$\hat{H}^{\text{QP}} := \hat{H}^{\text{TB}} + \delta\Sigma, \quad (10)$$

and the corresponding QP equation that yields the QP energies $E_{m\mathbf{k}}^{\text{QP}}$ and wave functions $\psi_{m\mathbf{k}}^{\text{QP}}$ reads

$$(\hat{H}^{\text{TB}} + \delta\Sigma) \psi_{m\mathbf{k}}^{\text{QP}}(\mathbf{r}) = E_{m\mathbf{k}}^{\text{QP}} \psi_{m\mathbf{k}}^{\text{QP}}(\mathbf{r}). \quad (11)$$

In order to express the QP equation [Eq. (11)] as a matrix equation, we expand the QP wave functions in the basis of the TB wave functions $\psi_{n\mathbf{k}}^{\text{TB}}$,

$$\psi_{m\mathbf{k}}^{\text{QP}}(\mathbf{r}) = \sum_n d_n(m, \mathbf{k}) \psi_{n\mathbf{k}}^{\text{TB}}(\mathbf{r}). \quad (12)$$

In that basis, Eq. (11) becomes

$$\sum_{n'} \underbrace{[E_{n\mathbf{k}}^{\text{TB}} \delta_{n,n'} + \delta\Sigma_{n,n'}(\mathbf{k})]}_{\hat{H}_{n,n'}^{\text{QP}}(\mathbf{k})} d_{n'}(m, \mathbf{k}) = E_{m\mathbf{k}}^{\text{QP}} d_m(m, \mathbf{k}). \quad (13)$$

A practical calculation within the TB+ $\delta\Sigma$ method is done in three consecutive steps. First, we compute the energies $E_{n\mathbf{k}}^{\text{TB}}$ and wave functions $\psi_{n\mathbf{k}}^{\text{TB}}$ of the TB Hamiltonian \hat{H}^{TB} . In the second step, we construct the image self-energy operator from the TB wave functions (see Sec. II C). Finally, we set up the QP equation in the basis of the TB wave functions [Eq. (13)] and solve it by diagonalizing the QP Hamiltonian. In addition to the energies $E_{m\mathbf{k}}^{\text{QP}}$, diagonalizing the Hamiltonian also yields new wave functions $\psi_{m\mathbf{k}}^{\text{QP}}$ [Eq. (12)]. It turns out that the nonperturbative treatment of the image self-energy, including the update of wave functions, can be a crucial factor to obtain reliable results because of the spatial structure of the image self-energy.

C. Building the image self-energy operator in tight binding

To set up the QP equation [Eq. (13)] of the TB+ $\delta\Sigma$ method, it is necessary to represent the image self-energy operator $\delta\Sigma$ as a matrix in the basis of the TB wave functions. According to Eq. (7), this requires to calculate the matrix elements of the screened image interaction W_{im} in that basis.

In TB, the wave functions $\psi_{n\mathbf{k}}$ are expanded in a minimal Bloch basis $\{\chi_{\alpha\nu\mathbf{k}}\}$ constructed from atomic orbitals ϕ_α ,

$$\chi_{\alpha\nu\mathbf{k}}(\mathbf{r}) = \frac{1}{\sqrt{N}} \sum_{\mathbf{R}} e^{i\mathbf{k}(\mathbf{R}+\boldsymbol{\tau}_\nu)} \phi_\alpha(\mathbf{r} - \mathbf{R} - \boldsymbol{\tau}_\nu), \quad (14a)$$

$$\psi_{n\mathbf{k}}(\mathbf{r}) = \sum_{\alpha\nu} c_{\alpha\nu}(n, \mathbf{k}) \chi_{\alpha\nu\mathbf{k}}(\mathbf{r}). \quad (14b)$$

Here, N is the number of unit cells in the crystal, \mathbf{R} is a lattice vector of the Bravais lattice, $\boldsymbol{\tau}_\nu$ gives the position of the ν th

basis atom within the unit cell of the crystal, α labels the atomic orbitals centered at atom ν , and $c_{\alpha\nu}$ are the expansion coefficients of the wave functions. Using Eqs. (14a) and (14b), the matrix elements of the screened image interaction become

$$\langle n\mathbf{k}|W_{\text{im}}|n'\mathbf{k}\rangle = \sum_{\alpha\nu} \sum_{\alpha'\nu'} c_{\alpha\nu}^*(n, \mathbf{k}) c_{\alpha'\nu'}(n', \mathbf{k}) \langle \chi_{\alpha\nu\mathbf{k}}|W_{\text{im}}|\chi_{\alpha'\nu'\mathbf{k}}\rangle, \quad (15)$$

where

$$\begin{aligned} \langle \chi_{\alpha\nu\mathbf{k}}|W_{\text{im}}|\chi_{\alpha'\nu'\mathbf{k}}\rangle &= \sum_{\mathbf{R}} e^{i\mathbf{k}(\mathbf{R}-\boldsymbol{\tau}_\nu+\boldsymbol{\tau}_{\nu'})} \int \phi_\alpha^*(\mathbf{r}-\boldsymbol{\tau}_\nu) \\ &\times W_{\text{im}}(\mathbf{r}) \phi_{\alpha'}(\mathbf{r}-\mathbf{R}-\boldsymbol{\tau}_{\nu'}) d^3r. \end{aligned} \quad (16)$$

A difficulty in evaluating the expression in Eq. (16) arises from the fact that the atomic orbitals are not explicitly defined in semi-empirical TB. To overcome this problem, we use a point-charge approximation,

$$\begin{aligned} &\int \phi_\alpha^*(\mathbf{r}-\boldsymbol{\tau}_\nu) W_{\text{im}}(\mathbf{r}) \phi_{\alpha'}(\mathbf{r}-\mathbf{R}-\boldsymbol{\tau}_{\nu'}) d^3r \\ &\approx \frac{1}{2} [W_{\text{im}}(\boldsymbol{\tau}_\nu) + W_{\text{im}}(\boldsymbol{\tau}_{\nu'})] \\ &\times \int \phi_\alpha^*(\mathbf{r}-\boldsymbol{\tau}_\nu) \phi_{\alpha'}(\mathbf{r}-\mathbf{R}-\boldsymbol{\tau}_{\nu'}) d^3r, \end{aligned} \quad (17)$$

in which the integral of Eq. (16) is reduced to the overlap of the atomic orbitals. Here, we have used the fact that $W_{\text{im}}(\mathbf{R}+\boldsymbol{\tau}_{\nu'}) = W_{\text{im}}(\boldsymbol{\tau}_{\nu'})$. The expression for the matrix elements of the screened image interaction in the Bloch basis thus simplifies to

$$\begin{aligned} \langle \chi_{\alpha\nu\mathbf{k}}|W_{\text{im}}|\chi_{\alpha'\nu'\mathbf{k}}\rangle &\approx \frac{1}{2} \langle \chi_{\alpha\nu\mathbf{k}}|\chi_{\alpha'\nu'\mathbf{k}}\rangle [W_{\text{im}}(\boldsymbol{\tau}_\nu) + W_{\text{im}}(\boldsymbol{\tau}_{\nu'})] \\ &= \frac{S_{\alpha\nu, \alpha'\nu'}(\mathbf{k})}{2} [W_{\text{im}}(\boldsymbol{\tau}_\nu) + W_{\text{im}}(\boldsymbol{\tau}_{\nu'})]. \end{aligned} \quad (18)$$

In the above equation $S_{\alpha\nu, \alpha'\nu'}(\mathbf{k})$ is the overlap between the corresponding Bloch states.

In the point-charge approximation, the matrix elements of the screened image interaction between TB wave functions [Eq. (15)] become

$$\begin{aligned} \langle n\mathbf{k}|W_{\text{im}}|n'\mathbf{k}\rangle &= \frac{1}{2} \sum_{\alpha\nu} \sum_{\alpha'\nu'} c_{\alpha\nu}^*(n, \mathbf{k}) S_{\alpha\nu, \alpha'\nu'}(\mathbf{k}) c_{\alpha'\nu'}(n', \mathbf{k}) \\ &\times [W_{\text{im}}(\boldsymbol{\tau}_\nu) + W_{\text{im}}(\boldsymbol{\tau}_{\nu'})]. \end{aligned} \quad (19)$$

By introducing generalized Mulliken charges [36] for each atom site ν ,

$$\begin{aligned} q_\nu^{nn'}(\mathbf{k}) &= \frac{1}{2} \sum_{\alpha} \sum_{\alpha'\nu'} [c_{\alpha\nu}^*(n, \mathbf{k}) S_{\alpha\nu, \alpha'\nu'}(\mathbf{k}) c_{\alpha'\nu'}(n', \mathbf{k}) \\ &+ c_{\alpha'\nu'}^*(n, \mathbf{k}) S_{\alpha'\nu', \alpha\nu}(\mathbf{k}) c_{\alpha\nu}(n', \mathbf{k})], \end{aligned} \quad (20)$$

we can rewrite Eq. (19) in the compact form

$$\langle n\mathbf{k}|W_{\text{im}}|n'\mathbf{k}\rangle = \sum_{\nu} q_\nu^{nn'}(\mathbf{k}) W_{\text{im}}(\boldsymbol{\tau}_\nu). \quad (21)$$

The generalized Mulliken charge $q_\nu^{nn'}(\mathbf{k})$ can be regarded as a localized fractional point-charge, arising from the overlap of the TB wave functions $\psi_{n\mathbf{k}}$ and $\psi_{n'\mathbf{k}}$ in the region of atom ν .

Finally, substituting Eq. (21) into Eq. (7) leads to the following expression for the matrix elements of the image self-energy operator:

$$\delta\Sigma_{n,n'}(\mathbf{k}) = \begin{cases} -\frac{1}{2} \sum_{\nu} q_\nu^{nn'}(\mathbf{k}) W_{\text{im}}(\boldsymbol{\tau}_\nu) & \text{for } n, n' \in \text{occ.} \\ +\frac{1}{2} \sum_{\nu} q_\nu^{nn'}(\mathbf{k}) W_{\text{im}}(\boldsymbol{\tau}_\nu) & \text{for } n, n' \in \text{unocc.} \end{cases}. \quad (22)$$

The form of Eq. (22) provides an intuitive physical picture of the image self-energy: It is built from the classical electrostatic self-energy of fractional point charges.

III. SCREENED IMAGE INTERACTION IN LAYERED MATERIALS

In the previous section, we have introduced the image self-energy to quantify the impact of the image charge effect on the electronic structure of solids. The essential ingredient for the calculation of the image self-energy is the screened image interaction W_{im} . In this section, we deal with the calculation of the screened image interaction in layered materials.

In the first part, Sec. III A, we describe a general scheme to map a layered crystal, composed of an arbitrary number of layers, onto a simple dielectric continuum model. From that model we then derive a general expression for the screened image interaction inside layered materials using macroscopic electrostatics. In Sec. III B, we investigate the spatial variation of the screened image interaction inside a layered material and address the thickness dependence. In the last part, Sec. III C, we validate the accuracy of the continuum model approach to the screened image interaction.

A. Dielectric continuum model

The calculation of the screened Coulomb interaction in a layered geometry using macroscopic electrostatics has been extensively described in the literature [11,34,37,38]. Most of the published work has dealt with isotropic dielectrics. Layered materials, however, are inherently anisotropic dielectrics: The layered crystal structure with strong in-plane bonds and weak van der Waals forces between the layers leads to high charge susceptibility within the layers but low susceptibility along the stacking direction. Many of these materials have a high in-plane lattice symmetry, meaning their dielectric properties are (only) uniaxially anisotropic. In the following, we consider a layered crystal with uniaxially anisotropic dielectric properties and derive an expression for the screened image interaction W_{im} inside that crystal. A complete solution to the screened Coulomb interaction in all regions along with a more detailed derivation—for the general case of two arbitrary dielectrics surrounding the layer—is given in the Appendix.

To calculate the screened image interaction in the framework of macroscopic electrostatics, we map the atomic crystal structure of the real system onto a dielectric continuum model. Figure 2 illustrates our procedure to construct the dielectric model system for an arbitrary layered crystal in vacuum. In the continuum model, we replace the entire layered crystal with a single homogeneous dielectric medium of thickness $L = Nd$, where N is the number of layers and d is the thickness of a single layer; for d , we use the layer-to-layer distance of the bulk crystal. The uniaxial anisotropy in the dielectric

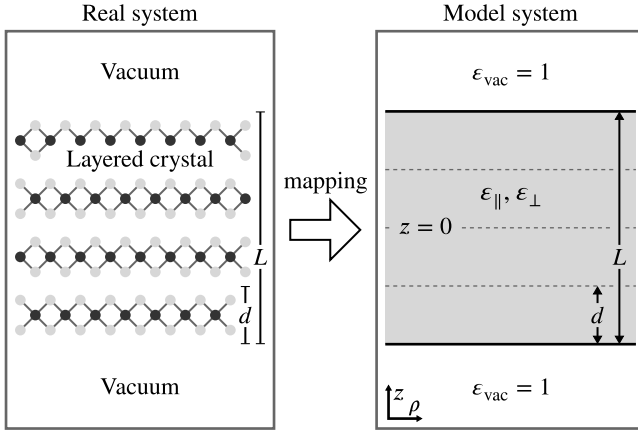


FIG. 2. Illustration of our procedure to map a layered crystal (left) onto a dielectric continuum model (right). The layered crystal is mapped to a single homogeneous medium of thickness $L = Nd$; N is the number of layers and d denotes the thickness of a single layer. The uniaxially anisotropic dielectric properties of the layered crystal are described by the two macroscopic dielectric constants, ϵ_{\parallel} and ϵ_{\perp} . Dielectric interfaces with the environment (black solid lines), here vacuum, are assumed to be abrupt.

properties of the layered material is taken into account in the model by the two macroscopic dielectric constants, ϵ_{\parallel} and ϵ_{\perp} . They represent the in-plane and out-of-plane dielectric response of the layered crystal, respectively; as before, we use the values of the bulk crystal. The vacuum above and below the layered crystal is characterized by a dielectric constant of $\epsilon_{\text{vac}} = 1$. We assume sharp dielectric interfaces between the layered crystal and the vacuum, meaning that the dielectric properties change abruptly at the interfaces. Finally, we note that internal interfaces within the layered crystal are not relevant in our model by construction.

Starting from the dielectric continuum model, we now derive an expression for the screened image interaction inside the layered crystal. To this end, we consider an additional/external point charge Q' at position $\mathbf{r}' = (\rho' = 0, z')$ inside the crystal, where we set $\rho' = 0$ without any loss in generality. We note, that this can be seen as a simplified picture of a QP excitation. Poisson's equation for the electrostatic potential ϕ in the region of the layered crystal reads (see Appendix)

$$\epsilon_{\parallel} \frac{1}{\rho} \frac{\partial}{\partial \rho} \left(\rho \frac{\partial \phi}{\partial \rho} \right) + \epsilon_{\perp} \frac{\partial^2 \phi}{\partial z^2} = -\frac{2}{\rho} Q' \delta(\rho) \delta(z - z'). \quad (23)$$

The solution to this equation can be written in the form $\phi = \phi_{\text{bulk}} + \phi_{\text{im}}$. The first term ϕ_{bulk} is the potential of the point charge in an infinite, uniaxially anisotropic, bulk crystal. ϕ_{bulk} is a *particular* solution of the inhomogeneous Poisson equation. The second term ϕ_{im} is the *image potential*. It is the solution of the Laplace equation obtained by setting the right-hand side of Eq. (23) to zero. Most importantly, the screened image interaction W_{im} between two point charges Q and Q' , located at \mathbf{r} and \mathbf{r}' inside the layered crystal, is related to the image potential by $W_{\text{im}}(\mathbf{r}, \mathbf{r}') = Q\phi_{\text{im}}(\mathbf{r})$.

In the following, we focus on the local part of the screened image interaction, relevant for the calculation of the image

TABLE I. Model parameters for the screened image interaction in MoS_2 . The thickness d of a single layer is the layer-to-layer distance of the bulk crystal, taken from Ref. [40]. The macroscopic dielectric constants, ϵ_{\parallel} (in-plane) and ϵ_{\perp} (out-of-plane), are calculated within *ab initio* LDA+GdW for bulk MoS_2 .

	Thickness d (Å)	Dielectric constants	
		ϵ_{\parallel} (in-plane)	ϵ_{\perp} (out-of-plane)
MoS_2	6.147	10.70	7.45

self-energy $\delta\Sigma$ [see Eqs. (7) and (22)]. By solving Poisson's equation (see Appendix), we obtain the following result for the local part of the screened image interaction inside a layered crystal surrounded by vacuum (in Hartree atomic units):

$$W_{\text{im}}(z) = \frac{1}{\gamma \epsilon_{\text{eff}}} \sum_{n=1}^{\infty} \frac{\xi^{2n}}{nL} + \frac{1}{\gamma \epsilon_{\text{eff}}} \sum_{n=0}^{\infty} \frac{\xi^{2n+1}}{|(2n+1)L + 2z|} + \frac{1}{\gamma \epsilon_{\text{eff}}} \sum_{n=0}^{\infty} \frac{\xi^{2n+1}}{|(2n+1)L - 2z|}. \quad (24)$$

In the above expression, $\epsilon_{\text{eff}} = \sqrt{\epsilon_{\parallel}\epsilon_{\perp}}$ is the effective macroscopic dielectric constant of the layered material and $\gamma = \sqrt{\epsilon_{\parallel}/\epsilon_{\perp}}$ quantifies the dielectric anisotropy [39]; furthermore, $\xi^n = [(\epsilon_{\text{eff}} - 1)/(\epsilon_{\text{eff}} + 1)]^n$ is the magnitude of the n th-order image charge.

Equation (24) plays a central role in our calculations—with the TB+ $\delta\Sigma$ method—presented in Sec. IV. We use this form of the screened image interaction to compute the matrix elements of the image self-energy. Generalization of Eq. (24) to the case of arbitrary dielectric environments is given in the Appendix. As we will show below, the screened image interaction [Eq. (24)] and hence the variation of dielectric screening due to the image charge effect can be calculated from the dielectric properties of the bulk crystal.

B. General features of the screened image interaction

It is useful to look at some general properties of the screened image interaction W_{im} as given in Eq. (24). As an illustrative example we consider the case of MoS_2 in vacuum. The model parameters we used for the calculation of the screened image interaction in MoS_2 are compiled in Table I.

Figure 3 shows the spatial variation of the screened image interaction along the stacking direction of freestanding MoS_2 for different numbers of layers (thickness). The qualitative behavior of the interaction is the same for all crystal thickness. The screened image interaction is positive in the whole region of the crystal, because of the smaller dielectric constant of the vacuum compared to MoS_2 . The energy curves are flat from the center of the crystal to about the second layer from the surface and then increase to finally diverge at the dielectric interfaces to the vacuum. Physically, the screened image interaction reflects the efficiency in dielectric screening relative to the bulk crystal. Positive values correspond to less effective screening; negative values would mean more effective screening. That is, the screened image interaction increases towards the surface(s) of the crystal due to the absence of

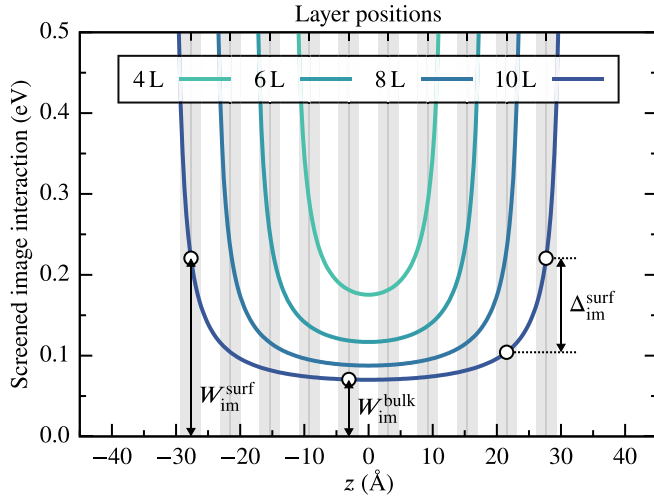


FIG. 3. Spatial variation of the screened image interaction in MoS₂ crystals of varying thickness (four to ten layers); all crystals are freestanding (surrounded by vacuum). The solid curves depict the image interaction energy $W_{\text{im}}(z)$ as resulting from Eq. (24), using the model parameters compiled in Table I. Arrows indicate characteristic values of the screened image interaction discussed in the text and shown in Table II. Gray regions mark the positions of the individual layers.

dielectric polarizability in the vacuum. Put another way, dielectric screening in the surface layer(s) is less effective compared to deeper layers.

The asymptotic divergencies of the screened image interaction when $|z| \rightarrow L/2$ are an artifact of the sharp dielectric interfaces or, equivalently, of the step discontinuities in the dielectric properties. We point out that these divergencies are unproblematic for the computation of the image self-energy in the TB+ $\delta\Sigma$ method [Eq. (22)], since their locations do not coincide with atomic positions by construction.

As is evident from Fig. 3, the screened image interaction monotonically decreases with increasing thickness (number of

TABLE II. Thickness-dependence of the screened image interaction in MoS₂ surrounded by vacuum. $W_{\text{im}}^{\text{bulk}}$, value at the center of the middle layer; $W_{\text{im}}^{\text{surf}}$, value at the center of the surface layer; $\Delta_{\text{im}}^{\text{surf}}$, difference between the values at the surface and the second layer. The crystal thickness of MoS₂ is given in terms of the number of layers. The model parameters used to compute the screened image interaction are listed in Table I.

Crystal thickness	$W_{\text{im}}^{\text{bulk}}$ (meV)	$W_{\text{im}}^{\text{surf}}$ (meV)	$\Delta_{\text{im}}^{\text{surf}}$ (meV)
1L	701	701	
2L	410	410	
4L	181	289	108
6L	119	251	114
8L	88	231	115
10L	70	220	116
20L	35	197	116
40L	18	186	116
∞L	0	175 ^a	117 ^a

^aComputed from the image potential in a half-space geometry, given in Ref. [39]

layers) of the crystal. For a more quantitative discussion of the thickness dependence, we focus on some characteristic values of the screened image interaction: (i) The energy $W_{\text{im}}^{\text{bulk}}$ at the center of the middle layer, (ii) the energy $W_{\text{im}}^{\text{surf}}$ at the center of the surface layer, and (iii) the difference in the energy $\Delta_{\text{im}}^{\text{surf}}$ between the surface and the second layer; see Fig. 3. Table II summarizes our computed values for MoS₂ in vacuum, with data covering the range from a monolayer (1L) up to a bulk crystal with surface (∞L). At small thicknesses the screened image interaction is quite substantial, with values in the range of several hundred meV. The values of $W_{\text{im}}^{\text{bulk}}$ and $W_{\text{im}}^{\text{surf}}$ both decrease as the number of layers increases. While the value in the center of the crystal goes to zero, the value in the surface layer approaches 175 meV. We find that both quantities are converged to within 20 meV at a thickness of 40 layers. The most interesting property of the screened image interaction is the value of $\Delta_{\text{im}}^{\text{surf}}$, since it gives the largest difference in the screened image interaction between two layers of the crystal. The value amounts to ~ 110 meV and is already converged better than 10 meV at a crystal thickness of four layers.

As discussed above, for a bulk crystal with the surface to vacuum (∞L), the screened image interaction in the surface layer does not approach zero but remains positive. For layers close to the surface, the absence of dielectric polarizability in the vacuum always leads to a reduced screening compared to the bulk counterpart, giving rise to the nonzero contribution of the image charge effect. From the image potential in a half-space geometry derived by Mele [39], we deduce the following expressions for the (local part of the) screened image interaction in the surface layer $W_{\text{im}}^{\text{surf}}$ and its difference between the surface and second layer $\Delta_{\text{im}}^{\text{surf}}$:

$$W_{\text{im}}^{\text{surf},(\infty\text{L})} = \frac{1}{\gamma} \frac{\epsilon_{\text{eff}} - 1}{\epsilon_{\text{eff}} \epsilon_{\text{eff}} + 1} \frac{1}{d}, \quad (25a)$$

$$\Delta_{\text{im}}^{\text{surf},(\infty\text{L})} = \frac{1}{\gamma} \frac{\epsilon_{\text{eff}} - 1}{\epsilon_{\text{eff}} \epsilon_{\text{eff}} + 1} \frac{2}{3d}. \quad (25b)$$

Note that these expressions correspond to the interface material-vacuum. Finally, we point out that magnitude and sign of Eqs. (25a) and (25b) depend on the dielectric contrast between the material and its environment (here, vacuum).

C. Comparison with *ab initio* results

To determine the accuracy of our macroscopically derived expression for the screened image interaction [Eq. (24)], we compare it to *ab initio* GW calculations on the direct band gap of monolayer MoS₂ in different dielectric environments. We begin by establishing a simple relation between the QP band gap and the screened image interaction. From the discussion of Sec. II we can write the QP band gap of the monolayer in the form

$$\begin{aligned} E_{\text{g}}(\zeta) &= E_{\text{g}}(\infty) + [\delta\Sigma_{\text{c}}(\zeta) - \delta\Sigma_{\text{v}}(\zeta)] \\ &= E_{\text{g}}(\infty) + \Delta E(\zeta), \end{aligned} \quad (26)$$

where $E_{\text{g}}(\infty)$ stands for the bulk-screened QP band gap and $\Delta E(\zeta)$ is the image self-energy correction induced due to the dielectric environment ζ of the monolayer; $\delta\Sigma_{\text{c}}(\zeta)$ and $\delta\Sigma_{\text{v}}(\zeta)$ are the image self-energy corrections of the conduction and valence state forming the band gap. In order to

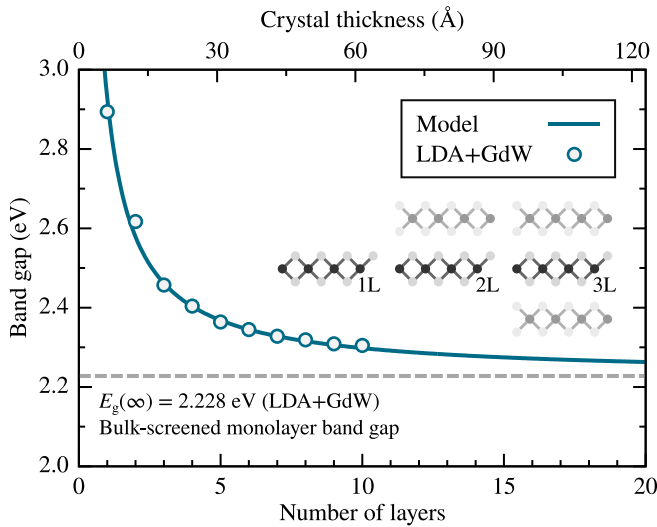


FIG. 4. Comparison of the screened image interaction (Model) and *ab initio* computed band gaps (LDA+GdW) of the innermost layer of a MoS₂ crystal in vacuum as a function of crystal thickness (number of layers). Since we neglected interlayer hopping within LDA+GdW, changes in the band gap are completely due to dielectric effects. The model gives the screened image interaction evaluated at the center of the crystal with the bulk-screened monolayer band gap (dashed line) as an additive offset [see Eq. (27)]. The parameters used to compute the screened image interaction are summarized in Table I.

simplify the comparison with the *ab initio* computed band gaps, we do not calculate $\delta\Sigma_c(\zeta)$ and $\delta\Sigma_v(\zeta)$ from the expectation value of the screened image interaction in the respective states [cf. Eq. (7)]; instead we simply evaluate the screened image interaction in the center of the monolayer, meaning at the height z_M of the molybdenum atoms. This is justified by the observation that the band edge states at the K point of monolayer MoS₂ mainly stem from localized *d* orbitals of the molybdenum atoms [3,41,42]. In this approximation, Eq. (26) simplifies to

$$E_g(\zeta) \approx E_g(\infty) + W_{\text{im}}(z_M; \zeta), \quad (27)$$

meaning that the *ab initio* computed band gap $E_g(\zeta)$ can be directly compared to the screened image interaction [up to the constant offset $E_g(\infty)$].

We use the LDA+GdW approximation [35] for the *ab initio* calculations, since it allows for a simple realization of arbitrary dielectric environments due to the usage of an atom-resolved model dielectric function. We point out that we have already successfully applied the LDA+GdW method to describe the electronic and optical properties of mono-, bilayer, and bulk crystals of several TMDCs [43–45].

In Fig. 4, we show the band gap of the innermost layer of a MoS₂ crystal as a function of crystal thickness. Quantum-mechanical interaction between the layers (interlayer hopping) is not taken into account, such that changes in the band gap are completely due to dielectric polarization effects. It is shown that the band gap of the innermost layer decreases with increasing thickness of the crystal: The polarizability of the other layers enhances the screening in the innermost layer, thereby reducing its band gap. Our results

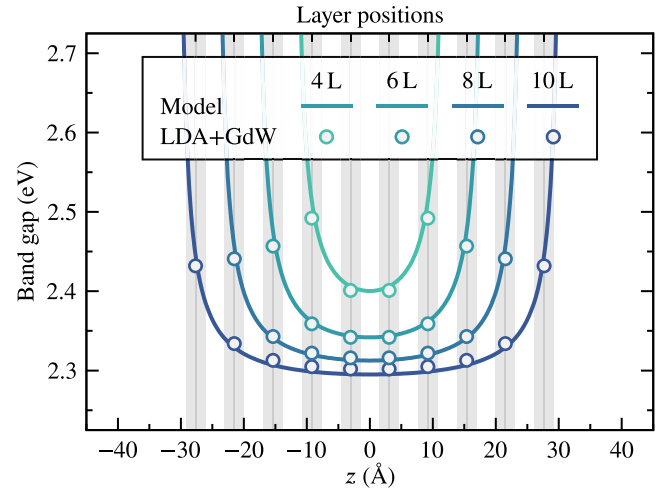


FIG. 5. Comparison of the spatial variation of the screened image interaction (Model) with *ab initio* computed band gaps (LDA+GdW) of the individual layers of a MoS₂ crystal in vacuum; quantum-mechanical interactions between the layers are neglected. Shown are the results for a crystal of four, six, eight, and ten layers. The curves of the model (screened image interaction) are the same as in Fig. 3, shifted by $E_g(\infty) = 2.228$ eV [see Eq. (27)]. The parameters used to compute the screened image interaction are listed in Table I.

obtained from the screened image interaction [Eq. (24)] are in good agreement with the *ab initio* results. The data shown in Fig. 4 give direct evidence that the image charge effect is the driving force behind the thickness dependence of self-energy corrections observed in layered materials such as black phosphorus [46], and TMDCs [47–49].

We have further calculated the variation of the band gap in MoS₂ crystals of different thickness as a function of the layer position. Figure 5 shows the position-dependent band gap for four crystals of different thickness; again, interlayer hopping is not taken into account. The closer the layers to the surface, the larger is their band gap. This effect can be explained with the absence of polarizability in the vacuum, which leads to weaker screening in layers close to the surface. The band gaps computed from the screened image interaction agree well with the *ab initio* ones for all crystal thickness.

We have shown that our macroscopic expression for the screened image interaction in layered materials, Eq. (24), provides a fairly good description of self-energy corrections caused by dielectric polarization effects; the image charge effect gives a simple explanation for these self-energy corrections. This justifies the use of Eq. (24) to calculate the matrix elements of the image self-energy operator $\delta\Sigma$ in the TB+ $\delta\Sigma$ method.

IV. IMAGE CHARGE EFFECT IN LAYERED MATERIALS

We now address the question of how the image charge effect affects the electronic structure of layered materials. Our main focus is set on the implications for the interlayer coupling in multilayer materials. By means of the TB+ $\delta\Sigma$ method, we can trace modifications in the electronic structure caused by the image charge effect in a direct way. Again, we use MoS₂ as a representative, as this material shows

TABLE III. Structural parameters of 2H-MoS₂ taken from Ref. [40].

	Lattice constants		Mo-S distance along z axis
	a (Å)	c (Å)	z_S (Å)
MoS ₂	3.160	12.294	1.586

pronounced interlayer interactions; these manifest themselves in the transition from a direct band gap in the monolayer to an indirect band gap in the bilayer and thicker crystals [3–5].

After a brief summary of the computational details in Sec. IV A, we first apply the TB+ $\delta\Sigma$ method to a monolayer in Sec. IV B. Then, in Sec. IV C, we apply the TB+ $\delta\Sigma$ method to a multilayer crystal to finally discuss the implications of the image charge effect on interlayer coupling.

A. Computational details

In order to compute the QP spectra and analyze the interplay between interlayer hopping and the image charge effect, we employ the TB+ $\delta\Sigma$ method. Starting point of our calculations is the nonorthogonal Slater-Koster TB model of Ref. [50]; a generic model that can accurately reproduce the DFT band structure of MoS₂, from a monolayer up to a bulk crystal. For the spin-orbit coupling, we use the parameters from Ref. [51] as they yield better agreement with our DFT band structure. Further, we use the structural parameters of 2H-MoS₂ reported in Ref. [40], which are listed in Table III; they correspond to averages computed from the results of several experiments. We switch to these structure parameters for consistency with the parameters for the screened image interaction (see below).

While quantum-mechanical interactions between the layers are already included in the Slater-Koster parameters of the TB model, the image charge effect is explicitly taken into account through the image self-energy in the TB+ $\delta\Sigma$ method. We use the parameters of Table I for the calculation of the screened image interaction.

Finally, we mention that all calculations in the present paper are carried out with a code implemented by ourselves.

B. Monolayer MoS₂

The monolayer provides a natural system to study the nature of the QP corrections caused by the image self-energy in the absence of quantum-mechanical interlayer interactions.

Figure 6 shows the band structure of monolayer MoS₂ in vacuum calculated with TB and with the TB+ $\delta\Sigma$ method. We aligned the band structures by setting the top of the valence band at the K point to 0 eV. As expected, the QP corrections of the image self-energy operator $\delta\Sigma$ lead to an increase of the band gap. The dispersion of the bands calculated with TB+ $\delta\Sigma$ closely follows that of the TB bands. The main effect of the image self-energy operator is a scissor shift of the bands. This is consistent with the results of Refs. [27] and [52]. Finally, we note that the wave functions of the monolayer within TB+ $\delta\Sigma$ are almost identical to the TB ones.

Figure 7 gives a different perspective on the effect of the image self-energy operator. Here, we plot the matrix elements

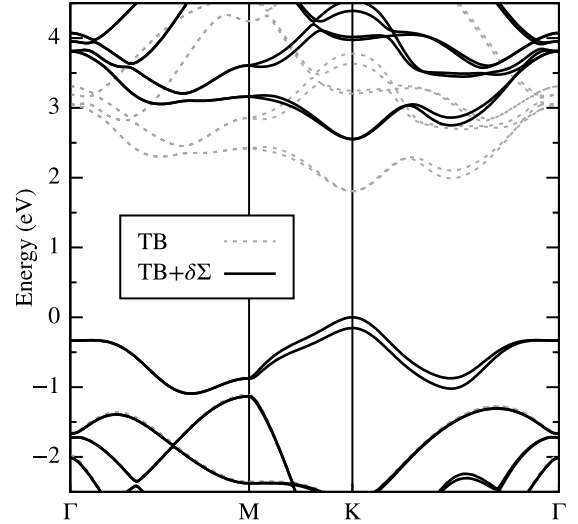


FIG. 6. Band structure of monolayer MoS₂ in vacuum computed with TB (thin dashed lines) and with TB+ $\delta\Sigma$ (thick solid lines). We aligned the band structures by setting the valence band edge at the K point to 0 eV. The main effect of the image self-energy operator $\delta\Sigma$ is to open the band gap from 1.8 eV in TB to 2.5 eV in TB+ $\delta\Sigma$.

or, equivalently, QP corrections $\langle\delta\Sigma\rangle$ of the image self-energy operator for the same system as before. The corrections are negative for valence band states and positive for conduction band states, with approximately the same magnitude. In both cases the corrections are almost constant, varying by less than 50 meV. This explains why the dispersion is almost preserved when going from TB to TB+ $\delta\Sigma$ (cf. Fig. 6), and once more

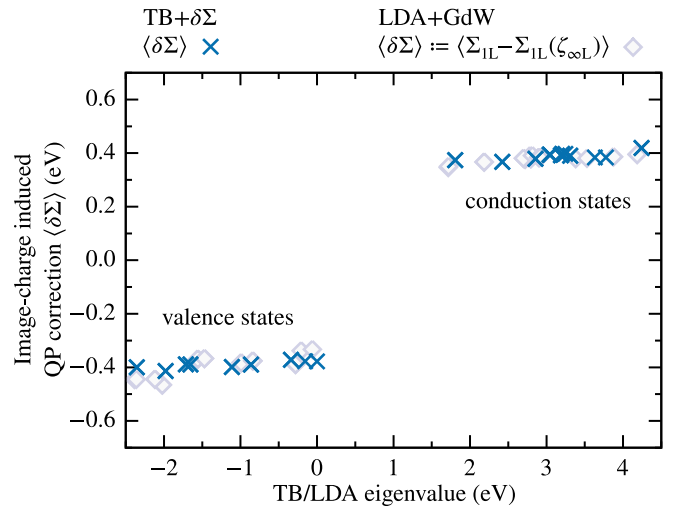


FIG. 7. Quasiparticle (QP) corrections caused by the image charge effect in a MoS₂ monolayer in vacuum. The crosses correspond to the corrections resulting from the image self-energy operator $\delta\Sigma$ in the TB+ $\delta\Sigma$ method; they are plotted against the TB energies. The diamonds correspond to the image-charge induced QP corrections resulting from the LDA+GdW method (see text); they are plotted against the LDA energies. The QP corrections were calculated at the high-symmetry points Γ , M, and K, of the first Brillouin zone.

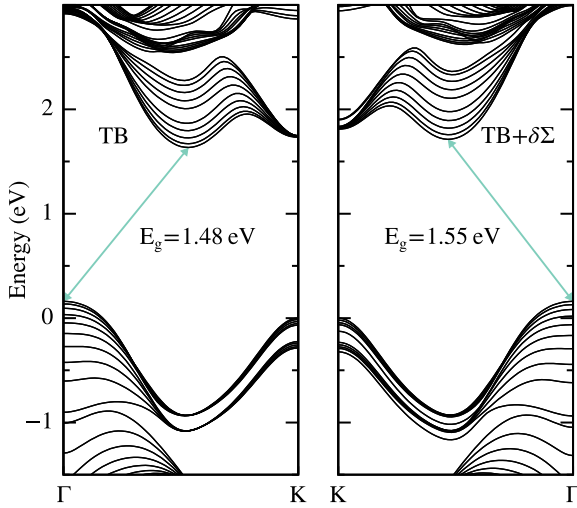


FIG. 8. Band structure of 10-layer MoS₂ in vacuum calculated with TB (left) and with the TB+ $\delta\Sigma$ method (right). Within both methods, the smallest band gap is formed between the valence band maximum at Γ and the conduction band minimum at Λ (halfway along ΓK). The QP corrections of the image self-energy operator $\delta\Sigma$ in TB+ $\delta\Sigma$ result in an increase of the band gap by 0.07 eV compared to TB.

shows that the main effect of $\delta\Sigma$ is a scissor shift. The (small) scattering in the QP corrections reflects the different spatial localization of the respective states. To further validate the effect of the image self-energy operator, we also show in Fig. 7 QP corrections computed with the *ab initio* LDA+GdW method. These corrections are evaluated for a monolayer in vacuum relative to a bulk-screened monolayer, for which one would obtain $\delta\Sigma = 0$. The good agreement between the corrections obtained from the two approaches justifies our approximations used in the evaluation of the image self-energy operator within the TB+ $\delta\Sigma$ method.

C. Multilayer MoS₂

In the following we consider 10-layer MoS₂ in vacuum, but similar results are obtained for other crystal sizes; the decisive factor is a layer number greater than two, so that the layers differ in terms of dielectric screening or, equivalently, in terms of the screened image interaction.

In Fig. 8, we compare the band structure of 10-layer MoS₂ calculated with TB and using the TB+ $\delta\Sigma$ method. The bands are shown along the high-symmetry line between Γ and K. Both calculations, TB and TB+ $\delta\Sigma$, reveal an indirect band gap with the valence band maximum at Γ and the conduction band minimum at Λ ; which is approximately halfway between Γ and K. However, the magnitude of the band gap increases from 1.48 eV in TB to 1.55 eV in TB+ $\delta\Sigma$. This increase in the band gap completely results from the image charge effect, not captured by the standard TB method. Note that we aligned both calculations by setting the valence band maximum at the K point to 0 eV.

In addition to the band gap renormalization, we observe changes in the band structure calculated using TB+ $\delta\Sigma$ that cannot be explained by a rigid shift uniform for all valence and

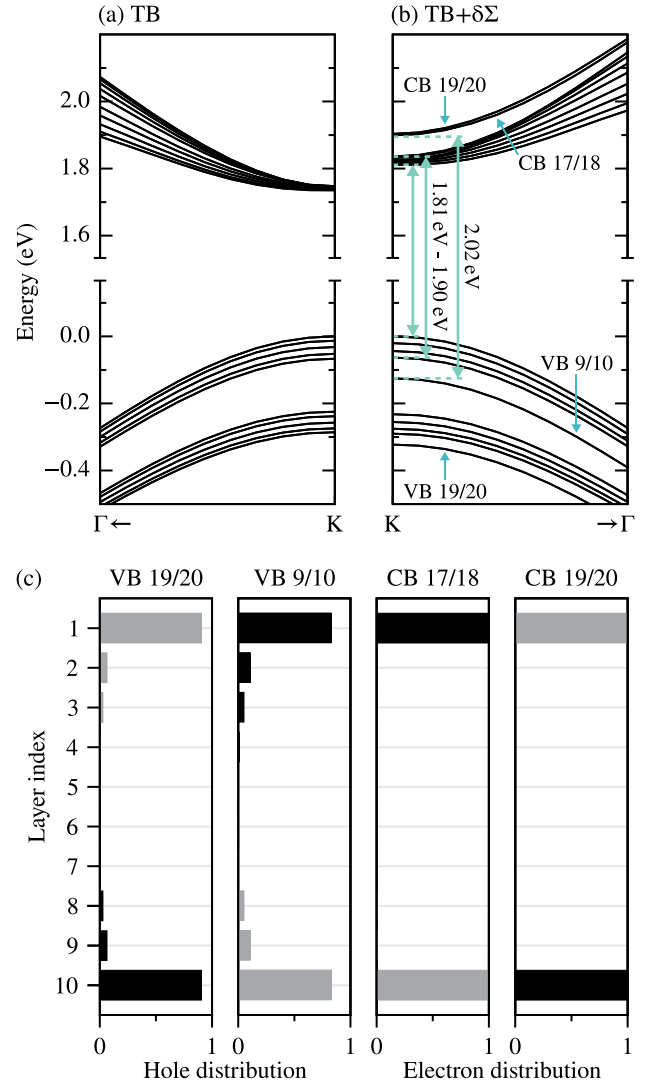


FIG. 9. Band structure of freestanding 10-layer MoS₂ in the region of the K point, computed with (a) TB and with (b) TB+ $\delta\Sigma$. Shown are the subbands of the two uppermost valence bands and the two lowermost conduction bands. All subbands are twofold degenerate, dictated by the symmetry of the system. The image charge effect—included in the TB+ $\delta\Sigma$ method—leads to an energetic decoupling of some subbands, labeled by small arrows. The wave functions of these energetically decoupled subbands (c) are strongly localized in one of the surface layers. The gray bars show the distribution of the spin-up polarized state and the black bars show the distribution of the spin-down polarized state of a pair of degenerate subbands; evaluated at the K point.

conduction bands. These changes are particularly pronounced around the K point and affect the topology of the subbands, which can be considered the fingerprint of interlayer coupling in layered materials. Figure 9 shows the subbands of 10-layer MoS₂ in the region of the direct band gap at the K point. We first review the picture that emerges from the TB calculations before turning to the changes in TB+ $\delta\Sigma$.

The valence bands shown in Fig. 9(a) cluster into two groups of ten subbands each. Note that only five subbands per group are visible because all subbands are twofold degenerate

due to the spatial inversion symmetry of the system. The groups originate from the two uppermost spin-split valence bands of the individual layers. The small energy splittings within each group of subbands come from interlayer interactions, while the much larger splitting between the groups results from a combination of interlayer interactions and (strong) spin-orbit coupling. The subbands from the two lowest conduction bands basically show the same picture as the valence bands. However, much weaker spin-orbit coupling and negligible interlayer interactions lead to more closely spaced subbands, specifically at the K point.

Remarkably, significant changes emerge in the pattern of the subbands in going from TB to TB+ $\delta\Sigma$ [cf. Figs. 9(a) and 9(b)]. In each group, one pair of degenerate subbands splits off and shifts to a distinctly different energy, away from the band gap. That is, these subbands decouple energetically from the other bands. In the valence bands, they shift to lower energies, while in the conduction bands they shift to higher energies.

In order to shed light on the energetic decoupling observed in TB+ $\delta\Sigma$, we analyze the wave functions of the respective subbands. Figure 9(c) shows the layer-resolved electron/hole distribution of the relevant subbands at the K point. The wave functions of all energetically decoupled subbands are strongly localized in the surface layer of the crystal. In contrast, the hole distributions obtained in TB resemble that of a quantum well, superimposed with a layer-by-layer oscillation due to the alternating spin-polarization of the bands (not shown). That is, the image charge effect leads to the formation of a surface-layer band gap at the K point. The surface-layer band gap amounts to 2.02 eV and is between 0.12 eV and 0.21 eV greater than the “bulk” band gap of the 10-layer crystal [see Fig. 9(b)].

As a final point, we emphasize that full diagonalization of the TB+ $\delta\Sigma$ Hamiltonian is mandatory to obtain physically meaningful results. Without diagonalization, the bands show unphysical dispersion at several points in the Brillouin zone.

The foregoing discussion demonstrates that the image charge effect can modify the interlayer coupling in MoS₂. The observed decoupling of the surface layer at the K point does not occur universally in the band structure, but rather shows a complicated wave vector and band dependence (cf. Fig. 8). For example, looking at the lowest conduction bands, the topology of the subbands changes drastically at the K point, while there are no significant changes near Λ . In the balance of this section, we examine how the image charge effect changes the interlayer coupling, and take up in more detail the variations of the surface layer (de-)coupling in MoS₂.

Interlayer coupling generally depends on two factors: The hopping matrix element between the layers, and the energy offset of their bands prior to coupling. To explore how the image charge effect modifies the interlayer coupling in MoS₂, we analyze the nature of the self-energy corrections within the TB+ $\delta\Sigma$ method. For this purpose, we express the image self-energy $\delta\Sigma$ of the multilayer crystal in the basis of the valence and conduction states of the individual layers before coupling. We shall refer to these states as *intralayer basis states*.

Using the aforementioned representation, we find that the image self-energy resembles a layer-resolved scissors operator for the intralayer basis states. The position-dependent magnitude of the scissors shift originates from the spatial

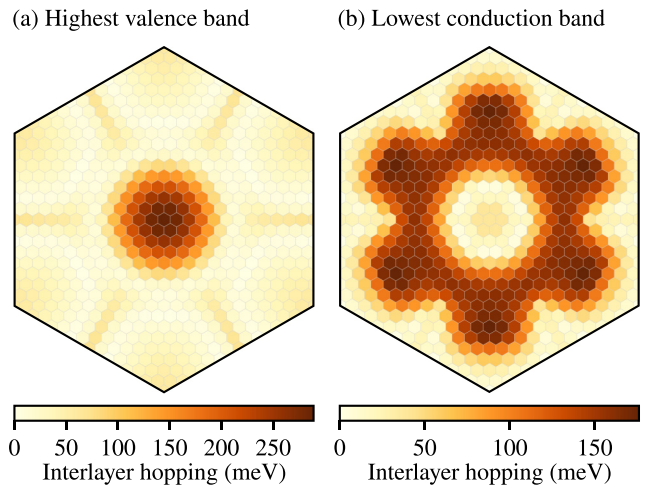


FIG. 10. Hopping matrix elements (interlayer hopping) between the surface layer and the second layer of 10-layer MoS₂. The interlayer hopping is shown for (a) the highest valence band and (b) the lowest conduction band, calculated with TB+ $\delta\Sigma$. Almost the same results are obtained with standard TB. The black hexagon outlines the area of the first Brillouin zone. We point out that top and bottom surface of the crystal yield the same results due to spatial inversion symmetry.

structure of the screened image interaction (cf. Sec. III B); the greatest shift occurs in the surface layer. Moreover, the representation of the image self-energy $\delta\Sigma$ in terms of intralayer basis states reveals that the hopping matrix elements between the layers remain almost unchanged. Consequently, the image charge effect modifies the interlayer coupling by altering the energy offset between the bands of the individual layers of the multilayer crystal prior to coupling.

To better understand the interlayer coupling in MoS₂ and to clarify the variations observed in the image-charge induced decoupling of the surface layer, we examine the interaction of the surface layer with the second layer by computing the hopping matrix elements between their intralayer basis states. Such matrix elements are also called *interlayer hopping* elements. Due to the spatial inversion symmetry of the system, the top and bottom surface of the crystal show the same results. Figures 10(a) and 10(b) show the interlayer hopping—calculated with the TB+ $\delta\Sigma$ method—for the highest valence band and the lowest conduction band in the entire Brillouin zone. In addition, Table IV gives a summary of the values at selected points of the Brillouin zone. We observe a strong

TABLE IV. Hopping matrix elements between the surface layer and the second layer of 10-layer MoS₂. The matrix elements were calculated with the TB+ $\delta\Sigma$ method, but almost the same results are obtained with standard TB. Results are listed for the highest valence band and the lowest conduction band at three selected points of the Brillouin zone. All energies are given in meV.

	Highest valence band	Lowest conduction band
Γ	290	40
Λ	5	165
K	60	0

variation of the interlayer hopping as a function of the wave vector and the band index, arising from the different orbital compositions of the relevant states. From a qualitative point of view, this explains the variations in the image charge-induced decoupling of the surface layer. We find that decoupling caused by the image charge effect only occurs in regions of weak interlayer hopping. For example, Table IV shows that interlayer hopping for the band edge states at the K point is small; for the lowest conduction band, interlayer hopping is forbidden by symmetry arguments [53]. This facilitates the decoupling of the surface layer through the image charge effect (i.e., through $\delta\Sigma$) at that point.

V. SUMMARY

In this paper, we have presented an efficient method to study the implications of dielectric screening effects of the environment (image charge effect) on the interlayer coupling in layered materials. The TB+ $\delta\Sigma$ method combines semi-empirical TB with a self-energy that accounts for interface-induced changes in the screened Coulomb interaction. We have demonstrated that these changes in the screened Coulomb interaction can be described by a simple dielectric continuum model. Using classical macroscopic electrostatics, we have derived a general expression for the screened image interaction in layered materials with uniaxially anisotropic dielectric properties.

We have presented results on the electronic structure of monolayer and multilayer MoS₂ surrounded by vacuum, calculated with the TB+ $\delta\Sigma$ method. In the case of the monolayer, the image charge effect caused a “scissors shift” of the valence and conduction bands, increasing the band gap by about 0.7 eV. In contrast, the self-energy corrections in the multilayer cannot be reduced to a scissors shift. We have found that, at the K point, the surface layer energetically decouples from the other layers. The image charge effect results in a formation of a surface-layer band gap that is about 0.2 eV larger than the smallest (“bulk”) band gap at that point. An analysis of the image self-energy revealed that the image charge effect modifies the interlayer coupling by changing the band offset between the layers. We further demonstrated that the interlayer hopping in MoS₂ strongly varies as a function of the wave vector and the band index, explaining the variations of the image-charge induced decoupling of the surface layer.

The energetic decoupling of the surface layer of MoS₂ at the K point of the Brillouin zone should be relevant in interpreting the results of surface-sensitive experiments such as two-photon photoemission spectroscopy [54]. More generally, our results suggest the possibility of “layer-selective” excitations in multilayer crystals.

In summary, we find that the TB+ $\delta\Sigma$ method provides an efficient way to study the image charge effect in mono- and multilayer materials. As a central result, we have found that the image charge effect can modify the interlayer coupling in layered materials.

ACKNOWLEDGMENT

This work has been funded by the Deutsche Forschungsgemeinschaft (DFG, German Research Foundation)–Project ID 223848855–SFB 1083 (Project No. A13).

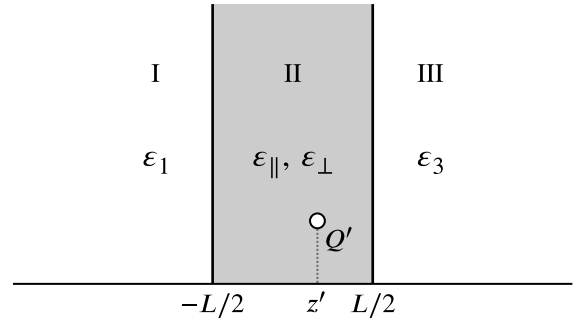


FIG. 11. A point charge inside a layer with uniaxially anisotropic dielectric properties (region II), sandwiched between two materials with different dielectric constants (regions I and III).

APPENDIX: SCREENED COULOMB INTERACTION INSIDE A LAYER WITH UNIAXIALLY ANISOTROPIC DIELECTRIC PROPERTIES

In this Appendix, we derive an expression for the screened Coulomb interaction of a point charge—a simplified picture of a QP excitation—inside a layer with uniaxially anisotropic dielectric properties. This also includes the expression for the screened image interaction given in Eq. (24); note that this equation (only) gives the local part. As a reminder, the screened image interaction describes the modification of the Coulomb interaction due to the dielectric environment of the layer. We derive the expressions within classical macroscopic electrostatics. Different from Sec. III A, here we consider the more general case of two different, arbitrary dielectrics surrounding the uniaxially anisotropic layer. Our derivation closely follows the work of Mele [39], who considered the case of a uniaxially anisotropic dielectric medium in a half-space geometry.

We consider the situation depicted in Fig. 11, where a point charge Q' is located at the position $\mathbf{r}' = (\rho' = 0, z')$ inside a layer of thickness L (region II). The dielectric properties of the layer are uniaxially anisotropic, with the dielectric constant for the in-plane and out-of-plane direction denoted by ϵ_{\parallel} and ϵ_{\perp} , respectively. The layer is sandwiched between two materials, each described by a different dielectric constant ϵ_1 (region I) and ϵ_3 (region III).

We begin with region II. The electrostatic potential inside the uniaxially anisotropic dielectric layer satisfies the Poisson equation (in Hartree atomic units)

$$\nabla^2 \phi_2(\mathbf{r}) = -4\pi Q' \delta(\mathbf{r} - \mathbf{r}') - 4\pi n_{\text{ind}}(\mathbf{r}), \quad (\text{A1})$$

where n_{ind} is the induced charge density within the layer. It is related to the potential ϕ_2 by

$$\begin{aligned} n_{\text{ind}}(\mathbf{r}) &= -\nabla \cdot \mathbf{P} \\ &= \nabla \chi \cdot \nabla \phi_2(\mathbf{r}). \end{aligned} \quad (\text{A2})$$

Here, \mathbf{P} is the polarization and χ is the susceptibility tensor of the layer. As the layer has uniaxially anisotropic dielectric properties, the susceptibility tensor can be expressed as

$$\chi = \begin{pmatrix} \chi_{\parallel} & 0 & 0 \\ 0 & \chi_{\parallel} & 0 \\ 0 & 0 & \chi_{\perp} \end{pmatrix}. \quad (\text{A3})$$

By substituting Eqs. (A2) and (A3) into Eq. (A1), Poisson's equation for the potential inside the layer takes the form

$$\varepsilon_{\parallel} \frac{1}{\rho} \frac{\partial}{\partial \rho} \left(\rho \frac{\partial \phi_2}{\partial \rho} \right) + \varepsilon_{\perp} \frac{\partial^2 \phi_2}{\partial z^2} = -\frac{2}{\rho} Q' \delta(\rho) \delta(z - z'). \quad (\text{A4})$$

Note that Eq. (A4) is given in cylindrical coordinates. The macroscopic dielectric constants ε_{\parallel} and ε_{\perp} , which we have introduced in Eq. (A4), are connected to the diagonal elements of the susceptibility tensor by the following relations:

$$\varepsilon_{\parallel} = 1 + 4\pi \chi_{\parallel}, \quad (\text{A5a})$$

$$\varepsilon_{\perp} = 1 + 4\pi \chi_{\perp}. \quad (\text{A5b})$$

In the regions above and below the layer, i.e., regions I and III, the Poisson equation for the electrostatic potential reduces to the Laplace equation (in cylindrical coordinates)

$$\left(\frac{\partial^2}{\partial \rho^2} + \frac{1}{\rho} \frac{\partial}{\partial \rho} + \frac{\partial^2}{\partial z^2} \right) \phi_{1/3}(\rho, z) = 0. \quad (\text{A6})$$

In order to solve Eqs. (A4) and (A6), we make use of the Hankel transform method. By applying the zero-order Hankel transform to the Poisson equation for the potential inside the layer [Eq. (A4)], we obtain

$$\left(\varepsilon_{\perp} \frac{\partial^2}{\partial z^2} - \varepsilon_{\parallel} q^2 \right) \tilde{\phi}_2(q, z) = -2Q' \delta(z - z'). \quad (\text{A7})$$

The solution to this equation can be expressed as

$$\tilde{\phi}_2(q, z) = \underbrace{F_+(q) e^{q\gamma(z+L/2)} + F_-(q) e^{-q\gamma(z-L/2)}}_{\tilde{\phi}_{\text{im}}} + \underbrace{\frac{Q'}{\varepsilon_{\text{eff}}} \frac{1}{q} e^{-q\gamma|z-z'|}}_{\tilde{\phi}_{\text{bulk}}}, \quad (\text{A8})$$

where $\varepsilon_{\text{eff}} = \sqrt{\varepsilon_{\parallel} \varepsilon_{\perp}}$ is the effective macroscopic dielectric constant of the uniaxially anisotropic layer, and $\gamma = \sqrt{\varepsilon_{\parallel} / \varepsilon_{\perp}}$ is an anisotropy parameter [39]. The first two terms on the right-hand side of Eq. (A8) correspond to the solution of the homogeneous portion of Poisson's equation; they constitute the *image potential*. The functions $F_+(q)$ and $F_-(q)$ will be determined by the present boundary conditions. The last term in Eq. (A8) is a particular solution of Poisson's equation and corresponds to the potential in case of an infinite bulk crystal. Turning to region I and III, the zero-order Hankel transform of the Laplace equation for the potential [Eq. (A6)] reads

$$\left(\frac{\partial^2}{\partial z^2} - q^2 \right) \tilde{\phi}_{1/3}(q, z) = 0. \quad (\text{A9})$$

The solution to this equation can be written in the form

$$\tilde{\phi}_{1/3}(q, z) = F_{1/3}(q) e^{\pm q(z \pm L/2)}, \quad (\text{A10})$$

where $F_1(q)$ and $F_3(q)$ will be determined by the boundary conditions; as above. The plus/minus sign in Eq. (A10) applies to the electrostatic potential in region I/III.

The present boundary conditions at the interfaces between the layer and its surrounding materials are

$$\mathbf{E}_{\parallel}^{(1)}(\rho, z = -L/2) = \mathbf{E}_{\parallel}^{(2)}(\rho, z = -L/2), \quad (\text{A11a})$$

$$\mathbf{E}_{\parallel}^{(3)}(\rho, z = +L/2) = \mathbf{E}_{\parallel}^{(2)}(\rho, z = +L/2), \quad (\text{A11b})$$

$$\mathbf{D}_{\perp}^{(1)}(\rho, z = -L/2) = \mathbf{D}_{\perp}^{(2)}(\rho, z = -L/2), \quad (\text{A11c})$$

$$\mathbf{D}_{\perp}^{(3)}(\rho, z = +L/2) = \mathbf{D}_{\perp}^{(2)}(\rho, z = +L/2). \quad (\text{A11d})$$

In the mixed-space representation—applying the zero-order Hankel transform—the boundary conditions can be written in the form

$$\tilde{\phi}_1(q, z = -L/2) = \tilde{\phi}_2(q, z = -L/2), \quad (\text{A12a})$$

$$\tilde{\phi}_3(q, z = +L/2) = \tilde{\phi}_2(q, z = +L/2), \quad (\text{A12b})$$

$$\varepsilon_1 \frac{\partial \tilde{\phi}_1}{\partial z} \Big|_{z=-L/2} = \varepsilon_{\perp} \frac{\partial \tilde{\phi}_2}{\partial z} \Big|_{z=-L/2}, \quad (\text{A12c})$$

$$\varepsilon_3 \frac{\partial \tilde{\phi}_3}{\partial z} \Big|_{z=+L/2} = \varepsilon_{\perp} \frac{\partial \tilde{\phi}_2}{\partial z} \Big|_{z=+L/2}. \quad (\text{A12d})$$

From these boundary conditions, we obtain

$$F_+(q) = \frac{Q'}{\varepsilon_{\text{eff}}} \frac{1}{q} \frac{\beta e^{-2q\gamma L}}{1 - \alpha\beta e^{-2q\gamma L}} [e^{q\gamma(z'+L/2)} + \alpha e^{-q\gamma(z'+L/2)}], \quad (\text{A13a})$$

$$F_-(q) = \frac{Q'}{\varepsilon_{\text{eff}}} \frac{1}{q} \frac{\alpha e^{-2q\gamma L}}{1 - \alpha\beta e^{-2q\gamma L}} [e^{-q\gamma(z'-L/2)} + \beta e^{q\gamma(z'-L/2)}], \quad (\text{A13b})$$

$$F_1(q) = \frac{Q'}{\varepsilon_{\text{eff}}} \frac{1}{q} \frac{(1 + \alpha) e^{-q\gamma L}}{1 - \alpha\beta e^{-2q\gamma L}} [e^{-q\gamma(z'-L/2)} + \beta e^{q\gamma(z'-L/2)}], \quad (\text{A13c})$$

$$F_3(q) = \frac{Q'}{\varepsilon_{\text{eff}}} \frac{1}{q} \frac{(1 + \beta) e^{-q\gamma L}}{1 - \alpha\beta e^{-2q\gamma L}} [e^{q\gamma(z'+L/2)} + \alpha e^{-q\gamma(z'+L/2)}]. \quad (\text{A13d})$$

The quantities α and β are defined by

$$\alpha = \frac{\varepsilon_{\text{eff}} - \varepsilon_1}{\varepsilon_{\text{eff}} + \varepsilon_1}, \quad \text{and} \quad \beta = \frac{\varepsilon_{\text{eff}} - \varepsilon_3}{\varepsilon_{\text{eff}} + \varepsilon_3}. \quad (\text{A14})$$

Substituting Eqs. (A13a)–(A13d) into Eqs. (A8) and (A10) gives the mixed-space representation of the potential inside and outside the uniaxially anisotropic layer.

To obtain the real-space expressions of the potentials, we calculate the inverse Hankel transform of Eqs. (A8) and (A10). For the interior potential, we find

$$\phi_2(\rho, z) = \phi_{\text{bulk}}(\rho, z) + \phi_{\text{im}}(\rho, z), \quad (\text{A15})$$

where ϕ_{bulk} is given by

$$\phi_{\text{bulk}}(\rho, z) = \frac{Q'}{\varepsilon_{\text{eff}}} \frac{1}{\sqrt{\rho^2 + \gamma^2(z-z')^2}} \quad (\text{A16})$$

and the image potential—solution to the homogeneous part of the Poisson equation [Eq. (A4)]—is given by

$$\begin{aligned} \phi_{\text{im}}(\rho, z) = & \frac{Q'}{\varepsilon_{\text{eff}}} \sum_{n=1}^{\infty} \left[\frac{(\alpha\beta)^n}{\sqrt{\rho^2 + \gamma^2(2nL + z - z')^2}} + \frac{(\alpha\beta)^n}{\sqrt{\rho^2 + \gamma^2(2nL - z + z')^2}} \right] \\ & + \frac{Q'}{\varepsilon_{\text{eff}}} \sum_{n=0}^{\infty} \left[\frac{\alpha^n \beta^{n+1}}{\sqrt{\rho^2 + \gamma^2((2n+1)L + z + z')^2}} + \frac{\alpha^{n+1} \beta^n}{\sqrt{\rho^2 + \gamma^2((2n+1)L - z - z')^2}} \right]. \end{aligned} \quad (\text{A17})$$

For the sake of completeness, we also give the expressions for the exterior potentials,

$$\begin{aligned} \phi_1(\rho, z) = & \frac{Q'}{\varepsilon_{\text{eff}}} (1 + \alpha) \sum_{n=0}^{\infty} \left[\frac{(\alpha\beta)^n}{\sqrt{\rho^2 + (\gamma\{2n+1\}L - z' + L/2) - z - L/2)^2}} \right. \\ & \left. + \frac{\alpha^n \beta^{n+1}}{\sqrt{\rho^2 + (\gamma\{2n+1\}L + z' - L/2) - z - L/2)^2}} \right], \end{aligned} \quad (\text{A18})$$

$$\begin{aligned} \phi_3(\rho, z) = & \frac{Q'}{\varepsilon_{\text{eff}}} (1 + \beta) \sum_{n=0}^{\infty} \left[\frac{(\alpha\beta)^n}{\sqrt{\rho^2 + (\gamma\{2n+1\}L - z' - L/2) + z - L/2)^2}} \right. \\ & \left. + \frac{\alpha^{n+1} \beta^n}{\sqrt{\rho^2 + (\gamma\{2n+1\}L + z' + L/2) + z - L/2)^2}} \right]. \end{aligned} \quad (\text{A19})$$

From these expressions, the individual contributions to the Coulomb interaction can be readily computed. For instance, the screened image interaction between a charge Q' at \mathbf{r}' and a charge Q at \mathbf{r} , both located inside the layer, is given by $W_{\text{im}}(\mathbf{r}, \mathbf{r}') = Q\phi_{\text{im}}(\mathbf{r})$.

Finally, to obtain the expression of Eq. (24) for the screened image interaction, we consider the special case of vacuum in region I and III. In this case, α and β take the same value

$$\xi \equiv \alpha = \beta = \frac{\varepsilon_{\text{eff}} - 1}{\varepsilon_{\text{eff}} + 1}. \quad (\text{A20})$$

Substituting this into Eq. (A17) and evaluating the screened image interaction at $\mathbf{r} = \mathbf{r}'$ —since we are only interested in the local part—we arrive at the expression given in Eq. (24).

-
- [1] Z. Shi, X. Wang, Y. Sun, Y. Li, and L. Zhang, Interlayer coupling in two-dimensional semiconductor materials, *Semicond. Sci. Technol.* **33**, 093001 (2018).
- [2] X. Wu, X. Chen, R. Yang, J. Zhan, Y. Ren, and K. Li, Recent advances on tuning the interlayer coupling and properties in van der Waals heterostructures, *Small* **18**, 2105877 (2022).
- [3] T. Li and G. Galli, Electronic Properties of MoS₂ nanoparticles, *J. Phys. Chem. C* **111**, 16192 (2007).
- [4] A. Splendiani, L. Sun, Y. Zhang, T. Li, J. Kim, C.-Y. Chim, G. Galli, and F. Wang, Emerging photoluminescence in monolayer MoS₂, *Nano Lett.* **10**, 1271 (2010).
- [5] K. F. Mak, C. Lee, J. Hone, J. Shan, and T. F. Heinz, Atomically Thin MoS₂: A New Direct-Gap Semiconductor, *Phys. Rev. Lett.* **105**, 136805 (2010).
- [6] K. Liu, L. Zhang, T. Cao, C. Jin, D. Qiu, Q. Zhou, A. Zettl, P. Yang, S. G. Louie, and F. Wang, Evolution of interlayer coupling in twisted molybdenum disulfide bilayers, *Nat. Commun.* **5**, 4966 (2014).
- [7] C. Zhang, C.-P. Chuu, X. Ren, M.-Y. Li, L.-J. Li, C. Jin, M.-Y. Chou, and C.-K. Shih, Interlayer couplings, Moiré patterns, and 2D electronic superlattices in MoS₂/WSe₂ hetero-bilayers, *Sci. Adv.* **3**, e1601459 (2017).
- [8] W.-T. Hsu, B.-H. Lin, L.-S. Lu, M.-H. Lee, M.-W. Chu, L.-J. Li, W. Yao, W.-H. Chang, and C.-K. Shih, Tailoring excitonic states of van der Waals bilayers through stacking configuration, band alignment, and valley spin, *Sci. Adv.* **5**, eaax7407 (2019).
- [9] P. Cudazzo, I. V. Tokatly, and A. Rubio, Dielectric screening in two-dimensional insulators: Implications for excitonic and impurity states in graphane, *Phys. Rev. B* **84**, 085406 (2011).
- [10] A. Chernikov, T. C. Berkelbach, H. M. Hill, A. Rigosi, Y. Li, B. Aslan, D. R. Reichman, M. S. Hybertsen, and T. F. Heinz, Exciton Binding Energy and Nonhydrogenic Rydberg Series in Monolayer WS₂, *Phys. Rev. Lett.* **113**, 076802 (2014).
- [11] M. Kumagai and T. Takagahara, Excitonic and nonlinear-optical properties of dielectric quantum-well structures, *Phys. Rev. B* **40**, 12359 (1989).
- [12] K. Tanaka, T. Takahashi, T. Kondo, T. Umebayashi, K. Asai, and K. Ema, Image charge effect on two-dimensional excitons in an inorganic-organic quantum-well crystal, *Phys. Rev. B* **71**, 045312 (2005).
- [13] J. B. Neaton, M. S. Hybertsen, and S. G. Louie, Renormalization of Molecular Electronic Levels at Metal-Molecule Interfaces, *Phys. Rev. Lett.* **97**, 216405 (2006).
- [14] J. M. Garcia-Lastra, C. Rostgaard, A. Rubio, and K. S. Thygesen, Polarization-induced renormalization of molecular levels at metallic and semiconducting surfaces, *Phys. Rev. B* **80**, 245427 (2009).
- [15] F. Hüser, T. Olsen, and K. S. Thygesen, Quasiparticle GW calculations for solids, molecules, and two-dimensional materials, *Phys. Rev. B* **87**, 235132 (2013).
- [16] Y. Lin, X. Ling, L. Yu, S. Huang, A. L. Hsu, Y.-H. Lee, J. Kong, M. S. Dresselhaus, and T. Palacios, Dielectric screening

- of excitons and trions in single-layer MoS₂, *Nano Lett.* **14**, 5569 (2014).
- [17] M. M. Ugeda, A. J. Bradley, S.-F. Shi, F. H. da Jornada, Y. Zhang, D. Y. Qiu, W. Ruan, S.-K. Mo, Z. Hussain, Z.-X. Shen *et al.*, Giant bandgap renormalization and excitonic effects in a monolayer transition metal dichalcogenide semiconductor, *Nat. Mater.* **13**, 1091 (2014).
- [18] A. J. Bradley, M. M. Ugeda, F. H. da Jornada, D. Y. Qiu, W. Ruan, Y. Zhang, S. Wickenburg, A. Riss, J. Lu, S.-K. Mo *et al.*, Probing the role of interlayer coupling and Coulomb interactions on electronic structure in few-layer MoSe₂ nanostructures, *Nano Lett.* **15**, 2594 (2015).
- [19] S. Latini, T. Olsen, and K. S. Thygesen, Excitons in van der Waals heterostructures: The important role of dielectric screening, *Phys. Rev. B* **92**, 245123 (2015).
- [20] I. Kylänpää and H.-P. Komsa, Binding energies of exciton complexes in transition metal dichalcogenide monolayers and effect of dielectric environment, *Phys. Rev. B* **92**, 205418 (2015).
- [21] M. Rösner, C. Steinke, M. Lorke, C. Gies, F. Jahnke, and T. O. Wehling, Two-dimensional heterojunctions from nonlocal manipulations of the interactions, *Nano Lett.* **16**, 2322 (2016).
- [22] A. Raja, A. Chaves, J. Yu, G. Arefe, H. M. Hill, A. F. Rigosi, T. C. Berkelbach, P. Nagler, C. Schüller, T. Korn *et al.*, Coulomb engineering of the bandgap and excitons in two-dimensional materials, *Nat. Commun.* **8**, 15251 (2017).
- [23] M. Drüppel, T. Deilmann, P. Krüger, and M. Rohlfing, Diversity of trion states and substrate effects in the optical properties of an MoS₂ monolayer, *Nat. Commun.* **8**, 2117 (2017).
- [24] L. Li, J. Kim, C. Jin, G. J. Ye, D. Y. Qiu, F. H. da Jornada, Z. Shi, L. Chen, Z. Zhang, F. Yang, K. Watanabe *et al.*, Direct observation of the layer-dependent electronic structure in phosphorene, *Nat. Nanotechnol.* **12**, 21 (2017).
- [25] D. Y. Qiu, F. H. da Jornada, and S. G. Louie, Environmental screening effects in 2D materials: Renormalization of the bandgap, electronic structure, and optical spectra of few-layer black phosphorus, *Nano Lett.* **17**, 4706 (2017).
- [26] D. Van Tuan, M. Yang, and H. Dery, Coulomb interaction in monolayer transition-metal dichalcogenides, *Phys. Rev. B* **98**, 125308 (2018).
- [27] K. T. Winther and K. S. Thygesen, Band structure engineering in van der Waals heterostructures via dielectric screening: the G Δ W method, *2D Mater.* **4**, 025059 (2017).
- [28] L. Hedin, New method for calculating the one-particle Green's function with application to the electron-gas problem, *Phys. Rev.* **139**, A796 (1965).
- [29] M. S. Hybertsen and S. G. Louie, Electron correlation in semiconductors and insulators: Band gaps and quasiparticle energies, *Phys. Rev. B* **34**, 5390 (1986).
- [30] G. Onida, L. Reining, and A. Rubio, Electronic excitations: density-functional versus many-body Green's-function approaches, *Rev. Mod. Phys.* **74**, 601 (2002).
- [31] M. Lannoo, C. Delerue, and G. Allan, Screening in Semiconductor Nanocrystallites and Its Consequences for Porous Silicon, *Phys. Rev. Lett.* **74**, 3415 (1995).
- [32] C. Delerue, M. Lannoo, and G. Allan, Excitonic and Quasiparticle Gaps in Si Nanocrystals, *Phys. Rev. Lett.* **84**, 2457 (2000).
- [33] C. Delerue, G. Allan, and M. Lannoo, Dimensionality-Dependent Self-Energy Corrections and Exchange-Correlation Potential in Semiconductor Nanostructures, *Phys. Rev. Lett.* **90**, 076803 (2003).
- [34] C. Freysoldt, P. Eggert, P. Rinke, A. Schindlmayr, and M. Scheffler, Screening in two dimensions: GW calculations for surfaces and thin films using the repeated-slab approach, *Phys. Rev. B* **77**, 235428 (2008).
- [35] M. Rohlfing, Electronic excitations from a perturbative LDA + GdW approach, *Phys. Rev. B* **82**, 205127 (2010).
- [36] T. A. Niehaus, M. Rohlfing, F. Della Sala, A. Di Carlo, and T. Frauenheim, Quasiparticle energies for large molecules: A tight-binding-based Green's-function approach, *Phys. Rev. A* **71**, 022508 (2005).
- [37] N. S. Rytova, Screened potential of a point charge in a thin film, *Proc. MSU Phys. Astron.* **3**, 30 (1967).
- [38] L. V. Keldysh, Coulomb interaction in thin semiconductor and semimetal films, *Pis'ma Zh. Eksp. Teor. Fiz.* **29**, 716 (1979) [*JETP Lett.* **29**, 658 (1979)].
- [39] E. J. Mele, Screening of a point charge by an anisotropic medium: Anamorphoses in the method of images, *Am. J. Phys.* **69**, 557 (2001).
- [40] T. Böker, R. Severin, A. Müller, C. Janowitz, R. Manzke, D. Voß, P. Krüger, A. Mazur, and J. Pollmann, Band structure of MoS₂, MoSe₂, and α -MoTe₂: Angle-resolved photoelectron spectroscopy and *ab initio* calculations, *Phys. Rev. B* **64**, 235305 (2001).
- [41] L. F. Mattheiss, Band structures of transition-metal-dichalcogenide layer compounds, *Phys. Rev. B* **8**, 3719 (1973).
- [42] Q. H. Wang, K. Kalantar-Zadeh, A. Kis, J. N. Coleman, and M. S. Strano, Electronics and optoelectronics of two-dimensional transition metal dichalcogenides, *Nat. Nanotechnol.* **7**, 699 (2012).
- [43] M. Drüppel, T. Deilmann, J. Noky, P. Marauhn, P. Krüger, and M. Rohlfing, Electronic excitations in transition metal dichalcogenide monolayers from an LDA + GdW approach, *Phys. Rev. B* **98**, 155433 (2018).
- [44] M.-C. Heissenbüttel, P. Marauhn, T. Deilmann, P. Krüger, and M. Rohlfing, Nature of the excited states of layered systems and molecular excimers: Exciplex states and their dependence on structure, *Phys. Rev. B* **99**, 035425 (2019).
- [45] I. Niehues, P. Marauhn, T. Deilmann, D. Wigger, R. Schmidt, A. Arora, S. M. de Vasconcellos, M. Rohlfing, and R. Bratschitsch, Strain tuning of the Stokes shift in atomically thin semiconductors, *Nanoscale* **12**, 20786 (2020).
- [46] V. Tran, R. Soklaski, Y. Liang, and L. Yang, Layer-controlled band gap and anisotropic excitons in few-layer black phosphorus, *Phys. Rev. B* **89**, 235319 (2014).
- [47] H.-P. Komsa and A. V. Krasheninnikov, Effects of confinement and environment on the electronic structure and exciton binding energy of MoS₂ from first principles, *Phys. Rev. B* **86**, 241201(R) (2012).
- [48] A. Molina-Sánchez, D. Sangalli, K. Hummer, A. Marini, and L. Wirtz, Effect of spin-orbit interaction on the optical spectra of single-layer, double-layer, and bulk MoS₂, *Phys. Rev. B* **88**, 045412 (2013).
- [49] A. Arora, T. Deilmann, P. Marauhn, M. Drüppel, R. Schneider, M. R. Molas, D. Vaclavkova, S. Michaelis de Vasconcellos, M. Rohlfing, M. Potemski, and R. Bratschitsch, Valley-contrasting

- optics of interlayer excitons in Mo- and W-based bulk transition metal dichalcogenides, *Nanoscale* **10**, 15571 (2018).
- [50] F. Zahid, L. Liu, Y. Zhu, J. Wang, and H. Guo, A generic tight-binding model for monolayer, bilayer and bulk MoS₂, *AIP Adv.* **3**, 052111 (2013).
- [51] G.-B. Liu, W.-Y. Shan, Y. Yao, W. Yao, and D. Xiao, Three-band tight-binding model for monolayers of group-VIB transition metal dichalcogenides, *Phys. Rev. B* **88**, 085433 (2013).
- [52] L. Waldecker, A. Raja, M. Rösner, C. Steinke, A. Bostwick, R. J. Koch, C. Jozwiak, T. Taniguchi, K. Watanabe, E. Rotenberg, T. O. Wehling, and T. F. Heinz, Rigid Band Shifts in Two-Dimensional Semiconductors through External Dielectric Screening, *Phys. Rev. Lett.* **123**, 206403 (2019).
- [53] G.-B. Liu, D. Xiao, Y. Yao, X. Xu, and W. Yao, Electronic structures and theoretical modelling of two-dimensional group-VIB transition metal dichalcogenides, *Chem. Soc. Rev.* **44**, 2643 (2015).
- [54] R. Wallauer, P. Maruhn, J. Reimann, S. Zoerb, F. Kraus, J. Güdde, M. Rohlfing, and U. Höfer, Momentum-resolved observation of ultrafast interlayer charge transfer between the topmost layers of MoS₂, *Phys. Rev. B* **102**, 125417 (2020).